Monthly Notices of the ROYAL ASTRONOMICAL SOCIETY

MNRAS **499,** 1340–1355 (2020) doi:10.1093/mnras/staa2856
Advance Access publication 2020 September 21

Variability and parsec-scale radio structure of candidate compact symmetric objects

M. Orienti[1]★ and D. Dallacasa[1,2]

[1]*Istituto di Radioastronomia – INAF, Via P. Gobetti 101, I-40129 Bologna, Italy*
[2]*Dipartimento di Fisica e Astronomia, Università di Bologna, Via Gobetti 93/2, I-40129 Bologna, Italy*

Accepted 2020 September 11. Received 2020 September 9; in original form 2020 June 29

ABSTRACT

We report results on multiepoch Very Large Array (VLA) and pc-scale Very Long Baseline Array (VLBA) observations of candidate compact symmetric objects (CSOs) from the faint sample of high-frequency peakers. New VLBA observations could resolve the radio structure in about 42 per cent of the observed sources, showing double components that may be either mini-lobes or core-jet structures. Almost all the sources monitored by the VLA show some variability on time-scale of a decade, and only one source does not show any significant variation. In 17 sources, the flux density changes randomly as it is expected in blazars, and in four sources the spectrum becomes flat in the last observing epoch, confirming that samples selected in the GHz regime are highly contaminated by beamed objects. In 16 objects, the pc-scale and variability properties are consistent with a young radio source in adiabatic expansion, with a steady decrease of the flux density in the optically thin part of the spectrum, and a flux density increase in the optically thick part. For these sources, we estimate dynamical ages between a few tens to a few hundred years. The corresponding expansion velocity is generally between $0.1c$ and $0.7c$, similar to values found in CSOs with different approaches. The fast evolution that we observe in some CSO candidates suggests that not all the objects would become classical Fanaroff–Riley radio sources.

Key words: radiation mechanisms: non-thermal – galaxies: active – radio continuum: general.

1 INTRODUCTION

Individual radio source evolution is a field of research where most of the ingredients are known. However, many details are still poorly understood, and it is necessary to investigate how such ingredients interact and influence each other. In a scenario, where radio sources grow in a self-similar way, the evolutionary stage of each radio source originated by an active galactic nucleus depends on its linear size. Compact symmetric objects (CSOs), with a linear size, LS, < 1 kpc and a two-sided structure that is reminiscent of Fanaroff–Riley radio galaxies (Fanaroff & Riley 1974), are likely to represent radio sources in an early evolutionary stage (see e.g. Wilkinson et al. 1994; Readhead et al 1996). Following an evolutionary path, CSOs would become medium-sized objects (MSOs) with $1 <$ LS $<$ 15–20 kpc, which are the progenitors of classical Fanaroff–Riley radio sources (e.g. Fanti et al. 2001). This is supported by the estimate of kinematic and radiative ages: 10^2–10^3 yr for CSOs (see e.g. Murgia 2003; Polatidis & Conway 2003), 10^4 –10^6 yr for MSOs (Murgia et al. 1999) and 10^7 –10^8 yr for large radio galaxies (Orrú et al. 2010; Harwood et al. 2017).

Several evolution models (e.g. Fanti et al. 1995; Readhead et al 1996; Snellen et al. 2000a; An & Baan 2012) have been proposed to describe how the physical parameters, such as luminosity, linear size, and velocity, evolve as the radio emission deploys. However, various aspects concerning the early stages of the radio evolution predicted by the models do not match the observations. This indicates that the initial parameters considered in evolution models must be improved by a better knowledge of the physical conditions when the radio emission turns on. In particular, the interaction with the ambient medium may play a crucial role during the early stage of radio source evolution (e.g. Dallacasa et al. 2013; Morganti et al. 2013; Collier et al. 2018; Keim, Callingham & Röttgering 2019; Sobolewska et al. 2019).

To test the physical conditions soon after the onset of the radio emission, it is essential to define a fair sample of CSOs, large enough to be statistically sound. A correct classification requires targeted (sub-)parsec-scale observations that prove their double morphology and identify the core position. Another indirect way to search for CSOs is by the analysis of their radio spectrum. An empirical anticorrelation was found between the projected linear size and the peak frequency (e.g. O'Dea & Baum 1997): the smaller the source, the higher the peak frequency is. In this context, the youngest CSOs should be sought among those sources whose synchrotron spectrum peaks above a few GHz.

High-frequency peakers (HFPs; Dallacasa et al. 2000) are a heterogeneous class of extragalactic sources, mainly made of blazars and CSOs, and characterized by a radio spectrum that peaks above ∼5 GHz. With the aim of searching for CSOs, two samples of HFP radio sources in the Northern hemisphere have been constructed and are currently available: The 'bright' sample (sources brighter than 300 mJy at 5 GHz) selected by Dallacasa et al. (2000) and the 'faint' sample (sources with flux density between 50 and 300 mJy at 5 GHz around the North Galactic Cap) presented in Stanghellini,

★ E-mail: orienti@ira.inaf.it

Dallacasa & Orienti (2009), consisting of about 60 sources each. These samples were built starting from the NRAO VLA Sky Survey and 87 Green Bank (87GB) catalogues and selecting only those sources with a radio spectrum peaking at 5 GHz or above, and subsequently cleaned via quasi-simultaneous multifrequency observations with the Very Large Array (VLA). Further epochs of quasi-simultaneous multifrequency spectra were obtained to distinguish between CSO candidates from variable flat-spectrum sources that matched the initial selection criteria owing to their variability (Tinti et al. 2005; Torniainen et al. 2005; Hovatta et al. 2006; Sadler et al. 2006; Orienti, Dallacasa & Stanghellini 2007; Mingaliev et al. 2012). Moreover, all the objects from the bright sample and ∼30 per cent of those from the faint sample were imaged at parsec-scale resolution in order to determine their morphology (Orienti et al. 2006; Orienti & Dallacasa 2012). CSOs are not significantly variable (O'Dea 1998), possess low polarization, and have double/triple radio morphology characterized by mini-lobes/hotspots and relativistic beaming does not play a major role. On the other hand, blazars do possess strong variability across the whole electromagnetic spectrum, have high polarization, and have core-jet structures on pc-scales. However, in the youngest radio sources, substantial variability is expected as a consequence of the source expansion, on time-scales much longer than in beamed objects, and with modest amplitude. In newly born radio sources, a significant evolution of the radio emission can occur on time-scales of the order of a few decades. Assuming a homogeneous radio source in adiabatic expansion with the magnetic field frozen in the plasma, the flux density variation in the optically thick part of the spectrum is $\Delta S \propto (1 + (\Delta t/t_0))^3$, where t_0 is the source age and Δt is the time interval between two observations. If Δt is a large fraction of t_0, ΔS can be significant.

In this paper, we present results on new VLA observations from 1 to 32 GHz of 35 out of 61 sources from the faint HFP sample, and Very Long Baseline Array (VLBA) observations at 15 and 24 GHz of a sub-sample of 12 sources. The long time-baseline of multiepoch VLA observations (more than a decade) allows us to study the long-term variability and investigate if some spectral changes are consistent with a CSO in adiabatic expansion. On the other hand, dual-frequency observations with milliarcsecond resolution provide a deep look into the radio source structure at few parsecs in size. The combination of VLA and VLBA information is necessary for determining the nature of each object and removing blazars that contaminate the sample of CSO candidates. The final goal is the construction of a sample of genuinely young CSOs. The determination of the physical properties in the very early phase of radio source evolution will provide important constraints on the initial conditions assumed in the development of evolutionary models.

This paper is organized as follows. In Section 2, we present the observations and data analysis; results are reported in Section 3 and discussed in Section 4. A brief summary is presented in Section 5.

Throughout this paper, we assume the following cosmology: $H_0 = 71\ \mathrm{km\,s^{-1}\,Mpc^{-1}}$, $\Omega_\mathrm{M} = 0.27$, and $\Omega_\Lambda = 0.73$, in a flat Universe. The spectral index α is defined as $S(\nu) \propto \nu^{-\alpha}$.

2 RADIO OBSERVATIONS

2.1 VLA observations

Simultaneous multifrequency VLA observations of 35 out of the 61 sources from the 'faint' HFP sample (Stanghellini et al. 2009) were carried out during two runs in 2012 April and May (Table 1). Observations were performed in the *L* (1−2 GHz), *S* (2−4 GHz), *C* (4.5−6.5 GHz), *X* (8−10 GHz), *Ku* (13−15 GHz), and *K* (20.2−22.2 GHz) bands, and for a run also in the *Ka* (31−33 GHz) band (project code: 12A-048). Observations had a bandwidth of 2 GHz, with the exception of the *L* band. In each frequency band, the bandwidth was divided into 16 spectral windows. In both runs, 3C 286 was used as primary calibrator and bandpass calibrator, with the exception of *K* and *Ka* band, were the calibrator J0927 + 3902 (4C 39.25) was used as bandpass calibrator. Target sources were observed for about 1.5 min per frequency. Secondary calibrators were chosen to minimize the antenna slewing.

Table 1. Log of radio observations.

Date	Project	Configuration	Code
2012-4-25	AO281	VLA-C	a
2012-6-16	AO281	VLA-CnB	b
2019-1-19	BO057	VLBA	c

Calibration was performed using the `CASA` software (McMullin et al. 2007) following the standard procedure for the VLA. Parts of the *L*, *S*, and *C* bands were highly affected by RFI and we had to flag some spectral windows. Errors on the amplitude calibration are conservatively 3 per cent in the *L*, *C*, and *X* bands, 5 per cent in *Ku* band, and 10 per cent in the *S*, *K*, and *Ka* bands. After the a priori calibration, imaging was done with the `CASA` task `CLEAN` and the `AIPS` task `IMAGR`. Phase-only self-calibration of the target field was generally performed in the *L* band, given the presence of many sources in the field of view, granting a substantial amount of flux density for the model.

We produced an image for each spectral window of each band in order to maximize the spectral coverage (Fig. 1). In Table 2, we report the flux densities at 1.4, 1.7, 4.5, 5.0, 8.1, 8.4, 15, 22, and 32 GHz, in order to have a direct comparison with the values from the narrow-band receivers of historical VLA observations (Stanghellini et al. 2009; Orienti, Dallacasa & Stanghellini 2010). When RFI affects any of those frequencies, nothing is reported.

The error on the image plane, σ_rms, is usually around 50 $\mu\mathrm{Jy\,beam^{-1}}$, but it may be as high as 0.2−0.5 $\mathrm{mJy\,beam^{-1}}$ in some spectral windows particularly affected by RFI.

2.2 VLBA observations and data reduction

VLBA observations at 15 and 24 GHz of a sub-sample of 12 faint HFP sources were carried out on 2019 January 19 in dual polarization and an aggregate bit rate of 2Gbps (project code BO057). The target sources were selected on the basis of their peak frequency below 7 GHz, in order to have observations in the optically thin part of the spectrum.

Each source was observed for about 25 min at 15 GHz and for 30 min at 24 GHz, spread into 12–15 short scans of about 2 min each, switching between frequencies and sources in order to improve the coverage of the (*u, v*) plane. Target sources are too faint for fringe fitting, and the observations were performed in phase-referencing mode. Phase calibrators are reported in Table 3.

Calibration and data reduction were performed following the standard procedures described in the Astronomical Image Processing System (`AIPS`) cookbook. J0927 + 3902 was used to generate the bandpass correction. The amplitudes were calibrated using antenna system temperatures and antenna gains and applying an atmospheric opacity correction. The uncertainties on the amplitude calibration were found to be approximately 7 per cent at both frequencies.

Images were produced in `AIPS` with the task `IMAGR`. Phase-only self-calibration was performed for those sources stronger than 10

Table 2. Multifrequency VLA flux density of faint HFP sources.

Source (1)	ID (2)	z (3)	$S_{1.4}$ (4)	$S_{1.7}$ (5)	$S_{4.5}$ (6)	$S_{5.0}$ (7)	$S_{8.1}$ (8)	$S_{8.4}$ (9)	$S_{14.5}$ (10)	$S_{21.5}$ (11)	S_{32} (12)	α_b (13)	α_a (14)
J0754 + 3033	Q	0.769	66 ± 2	75 ± 2	142 ± 4	145 ± 4	143 ± 4	141 ± 4	108 ± 5	96 ± 10	–	−0.6	0.4
J0819 + 3823	Q	–	19 ± 1	25 ± 1	115 ± 3	118 ± 4	–	–	41 ± 2	25 ± 3	–	−1.5	1.1
J0821 + 3107	Q	2.625	96 ± 5	106 ± 5	71 ± 2	68 ± 2	52 ± 2	50 ± 2	34 ± 4	33 ± 5	–	–	0.5
J0951 + 3451	G	0.358	27 ± 1	36 ± 1	63 ± 2	64 ± 2	57 ± 2	56 ± 2	35 ± 2	27 ± 3	21 ± 2	−1.0	0.6
J0955 ± 3355	Q	2.491	46 ± 2	61 ± 3	68 ± 2	66 ± 2	47 ± 1	45 ± 1	26 ± 2	20 ± 3	–	−0.9	0.8
J1008 + 2533	Q	1.96	54 ± 3	69 ± 3	102 ± 3	105 ± 3	103 ± 3	104 ± 3	115 ± 6	130 ± 13	–	−1.1	0.0
J1020 + 4320	Q	1.964	117 ± 4	158 ± 5	306 ± 9	303 ± 9	243 ± 7	239 ± 7	161 ± 8	124 ± 12	–	−1.0	0.5
J1025 + 2541	G	0.457	26 ± 1	31 ± 1	42 ± 1	38 ± 1	23 ± 1	21 ± 1	11 ± 1	5 ± 1	–	−1.2	1.2
J1035 + 4230	Q	2.44	23 ± 1	28 ± 1	77 ± 2	88 ± 3	84 ± 3	83 ± 3	59 ± 3	40 ± 4	29 ± 3	−1.1	0.7
J1044 + 2959	Q	2.983	52 ± 2	66 ± 2	132 ± 4	134 ± 4	124 ± 4	123 ± 4	95 ± 5	75 ± 8	–	−0.8	0.5
J1046 + 2600	–	–	16 ± 1	20 ± 1	35 ± 1	33 ± 1	23 ± 1	22 ± 1	11 ± 1	6 ± 1	–	–1.1	1.1
J1052 + 3355	Q	1.407	–	23 ± 5	24 ± 1	22 ± 1	13 ± 1	11 ± 1	7 ± 1	6 ± 1	–	–	0.9
J1054 + 5058	Q	–	12 ± 1	13 ± 1	21 ± 1	21 ± 1	28 ± 1	30 ± 1	36 ± 2	–	–	−0.5	–
J1058 + 3353	G	0.265	–	21 ± 3	–	–	78 ± 2	80 ± 2	116 ± 6	118 ± 12	–	−0.7	–
J1107 + 3421	–	–	29 ± 1	42 ± 2	64 ± 2	60 ± 2	37 ± 1	35 ± 1	18 ± 1	9 ± 1	–	–1.4	1.1
J1137 + 3441	Q	0.835	13 ± 2	30 ± 3	59 ± 2	62 ± 2	63 ± 2	63 ± 2	61 ± 3	59 ± 6	–	−0.9	0.1
J1218 + 2828	G	0.18p	–	–	55 + 2	56 ± 2	41 ± 1	39 ± 1	29 ± 2	42 ± 4	–	−0.5	0.6
J1240 + 2323	G	0.38p	18 ± 5	24 ± 3	–	–	50 ± 2	50 ± 2	45 ± 1	42 ± 1	–	−0.6	0.2
J1240 + 2425	Q	0.831	63 ± 3	54 ± 3	30 ± 1	28 ± 1	18 ± 1	17 ± 1	10 ± 1	7 ± 1	–	–	0.9
J1258 ± 2820	Q	–	–	–	45 ± 2	49 ± 2	51 ± 2	51 ± 2	45 ± 2	34 ± 3	–	−0.3	0.5
J1309 + 4047	Q	2.91	–	62 ± 2	128 ± 4	127 ± 4	103 ± 3	101 ± 3	64 ± 3	37 ± 4	–	−0.9	0.7
J1420 + 2704	Q	–	–	19 ± 1	69 ± 3	70 ± 2	65 ± 2	64 ± 2	45 ± 2	29 ± 3	22 ± 2	−1.0	0.7
J1421 + 4645	Q	1.668	–	126 ± 4	237 ± 7	244 ± 7	244 ± 7	244 ± 4	204 ± 10	184 ± 18	136 ± 14	−0.7	0.4
J1459 + 3337	Q	0.645	50 ± 5	71 ± 5	216 ± 7	223 ± 7	188 ± 6	183 ± 6	108 ± 6	68 ± 7	43 ± 4	−1.0	1.0
J1512 + 2219	G	0.40p	14 ± 2	24 ± 3	24 ± 1	21 ± 1	10 ± 1	9 ± 1	3 ± 1	2 ± 1	–	−1.7	1.3
J1528 + 3816	Q	0.749	27 ± 1	32 ± 1	52 ± 2	53 ± 2	56 ± 2	57 ± 2	58 ± 6	57 ± 6	59 ± 6	−0.6	0.0
J1530 + 2705	G	0.033	24 ± 3	29 ± 3	50 ± 2	50 ± 2	41 ± 1	40 ± 1	28 ± 2	26 ± 3	–	−0.8	0.4
J1530 + 5137	G	0.632p	53 ± 2	60 ± 2	98 ± 3	100 ± 3	111 ± 3	112 ± 3	111 ± 6	115 ± 12	127 ± 13	−0.5	0.0
J1547 + 3518	Q	–	–	23 ± 2	41 ± 1	44 ± 1	51 ± 1	53 ± 2	53 ± 3	57 ± 6	–	−0.5	–
J1602 + 2646	G	0.372	–	44 ± 2	162 ± 5	189 ± 6	297 ± 9	310 ± 9	345 ± 17	303 ± 30	266 ± 27	−1.0	0.3
J1613 + 4223	Q	–	43 ± 1	70 ± 2	197 ± 6	188 ± 6	107 ± 3	102 ± 3	33 ± 3	15 ± 2	–	−1.9	1.6
J1616 + 4632	Q	0.950	82 ± 4	83 ± 4	77 ± 2	79 ± 2	78 ± 2	78 ± 2	62 ± 3	58 ± 6	–	–	0.2
J1617 + 3801	Q	1.607	26 ± 1	34 ± 1	72 ± 2	77 ± 2	115 ± 3	121 ± 4	128 ± 7	107 ± 11	83 ± 8	−1.0	0.4
J1624 + 2748	G	0.541p	19 ± 1	21 ± 1	97 ± 3	105 ± 3	155 ± 5	162 ± 5	175 ± 9	172 ± 17	153 ± 15	−1.2	–
J1719 + 4804	Q	1.084	70 ± 2	83 ± 3	83 ± 3	77 ± 2	47 ± 1	44 ± 1	18 ± 2	11 ± 1	–	−0.8	0.7

Notes. Column 1: source name; column 2: optical counterpart; column 3: redshift: a *p* indicates a photometric redshift; columns 4–12: flux density (in mJy) at 1.4, 1.7, 4.5, 5.0, 8.1, 8.4, 14.5, 21.5, and 32 GHz, respectively; columns 13 and 14: spectral index below and above the peak frequency, respectively.

Table 3. Pc-scale radio morphology and accurate source position of faint HFP sources with VLBA observations.

Source	M.	RA (J2000)	Dec. (J2000)	Cal. (B1950)
J0754 + 3033	CD	07:54:48.8514	30:33:55.020	0738 + 313
J0819 + 3823	CD	08:19:00.9562	38:23:59.810	0821 + 394
J1002 + 5701	Un	10:02:41.6661	57:01:11.484	1014 + 615
J1025 + 2541	CD	10:25:23.7918	25:41:58.362	1012 + 232
J1035 + 4230	MR	10:35:32.5776	42:30:18.959	1020 + 400
J1044 + 2959	Un	10:44:06.3428	29:59:01.004	1059 + 282
J1046 + 2600	MR	10:46:57.2508	26:00:45.104	1040 + 244
J1107 + 3421	CD	11:07:34.3382	34:21:18.596	1101 + 384
J1420 + 2704	Un	14:20:51.4879	27:04:27.045	1417 + 273
J1459 + 3337	CD	14:59:58.4359	33:37:01.776	1504 + 377
J1613 + 4223	Un	16:13:04.8033	42:23:18.893	1638 + 398
J1719 + 4804	Un	17:19:38.2496	48:04:12.248	1726 + 455

Notes. Column 1: source name; column 2: morphology – CD = compact double, MR = marginally resolved, and Un = unresolved. Columns 3 and 4: right ascension and declination of the main component; column 5: VLBA calibrator observed for phase referencing. The uncertainty on the position is about 0.16 mas.

mJy. The rms noise level on the image plane is between 0.07 and 0.3 mJy beam^{-1}. Flux densities are reported in Table 4. When the source is resolved we define E and W the eastern and western components, respectively (in Fig. 2 north is up and east is left).

The uncertainty on the source position was estimated by comparing the positions at 15 and 24 GHz, and it is about 0.16 mas.

3 RESULTS

The large bandwidth of the VLA observations allowed us to determine the spectral shape roughly continuously from 1 to 22 GHz, with only a few gaps among the *X*, *Ku,* and *K* bands. All the 35 sources are unresolved in the VLA images and we measured the flux densities using the task `JMFIT` in `AIPS` which performs a Gaussian fit on the image plane. In Fig. 1, we plot the flux densities for each spectral window, together with the measurements from earlier epochs as it is described in the caption.

VLBA observations could detect all the target sources at 15 and 24 GHz. Among the 12 sources observed with the VLBA, 7 sources (∼58 per cent) are resolved or marginally resolved on pc-scale. As in the case of VLA, for the unresolved sources, or unresolved components, we measured the flux density using the task

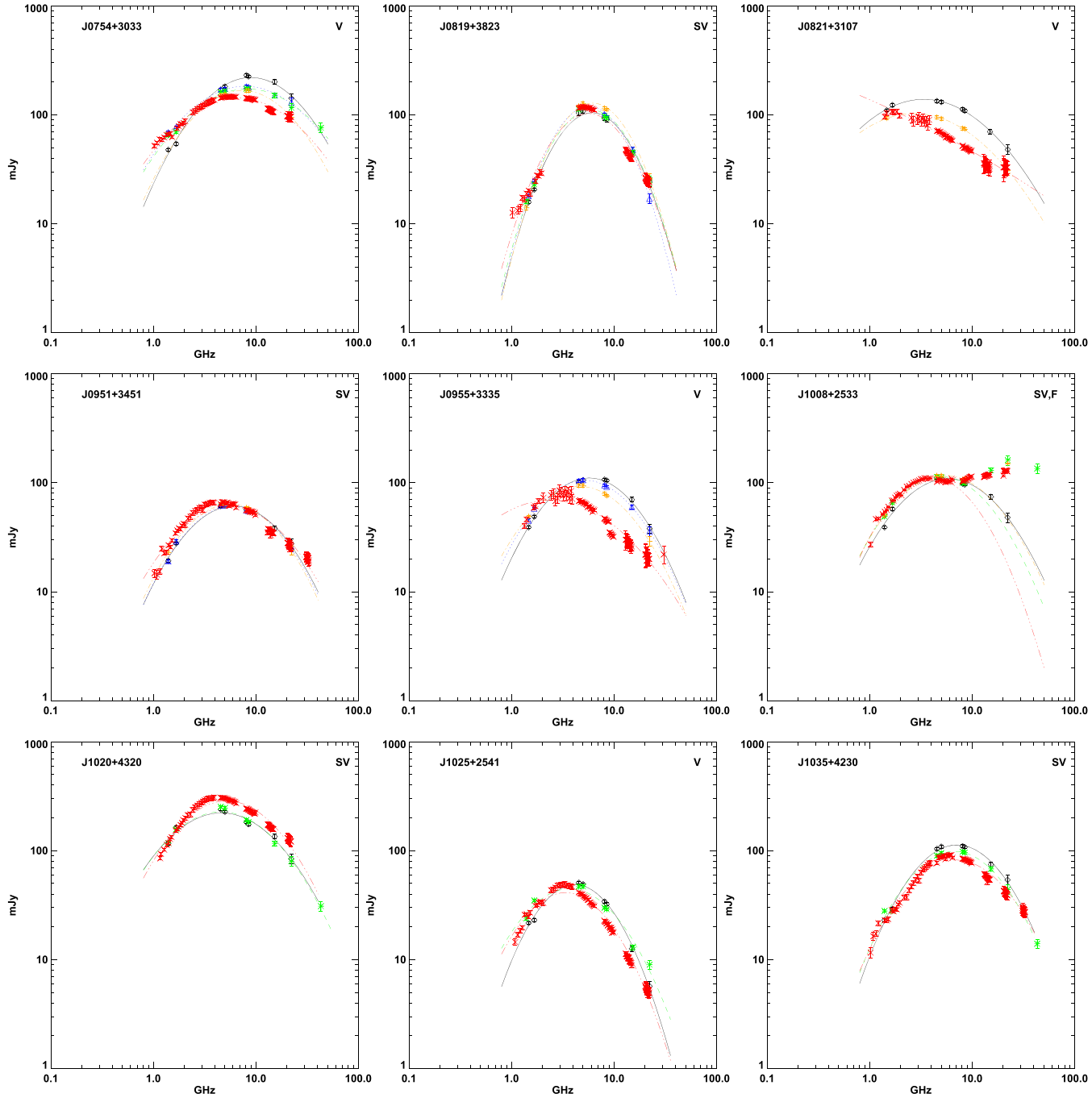

Figure 1. Radio spectra of the 35 HFPs from the 'faint' HFP sample observed with the VLA during the observing runs presented in this paper. Black diamonds and black solid line refer to the first epoch observations (1998–2000, Stanghellini et al. 2009); blue triangles and a blue dotted line refer to observations in 2003; green asterisks and a green dashed line refer to observations in 2004; orange + signs and orange dashed–dotted line refer to observations in 2006/2007; red crosses and red dashed–dotted line refer to the last epoch (2012). Flux densities and precise observing dates for the epoch 2003, 2004, and 2006–2007 can be found in Orienti & Dallacasa (2010). The designations V, SV, and NV mean that the source is classified as variable, slightly variable, and non-variable, respectively, while F indicates a flat radio spectrum during at least one epoch (see Section 3.2).

JMFIT, whereas for sources with complex structure we estimated the total flux density using TVSTAT, which extracts the flux density on a selected polygonal area on the image plane. Errors on the VLA and VLBA flux densities are estimated by $\sigma = \sqrt{\sigma_{\rm cal}^2 + \sigma_{\rm rms}^2}$, where $\sigma_{\rm cal}$ is the uncertainty on the amplitude calibration (see Section 2), and $\sigma_{\rm rms}$ is the 1σ noise level measured on the image plane. The former contribution is generally much larger than the latter.

Errors on the spectral index are computed assuming the error propagation theory:

$$\sigma_{\rm sp} = \sqrt{\left(\frac{\sigma_{S1}}{S_1}\right)^2 + \left(\frac{\sigma_{S2}}{S_2}\right)^2}\,\frac{1}{\ln(\nu_2) - \ln(\nu_1)},$$

where $S_{\rm i}$ and $\sigma_{\rm Si}$ are the flux density and the flux density error, respectively, at the frequency i (ν_i).

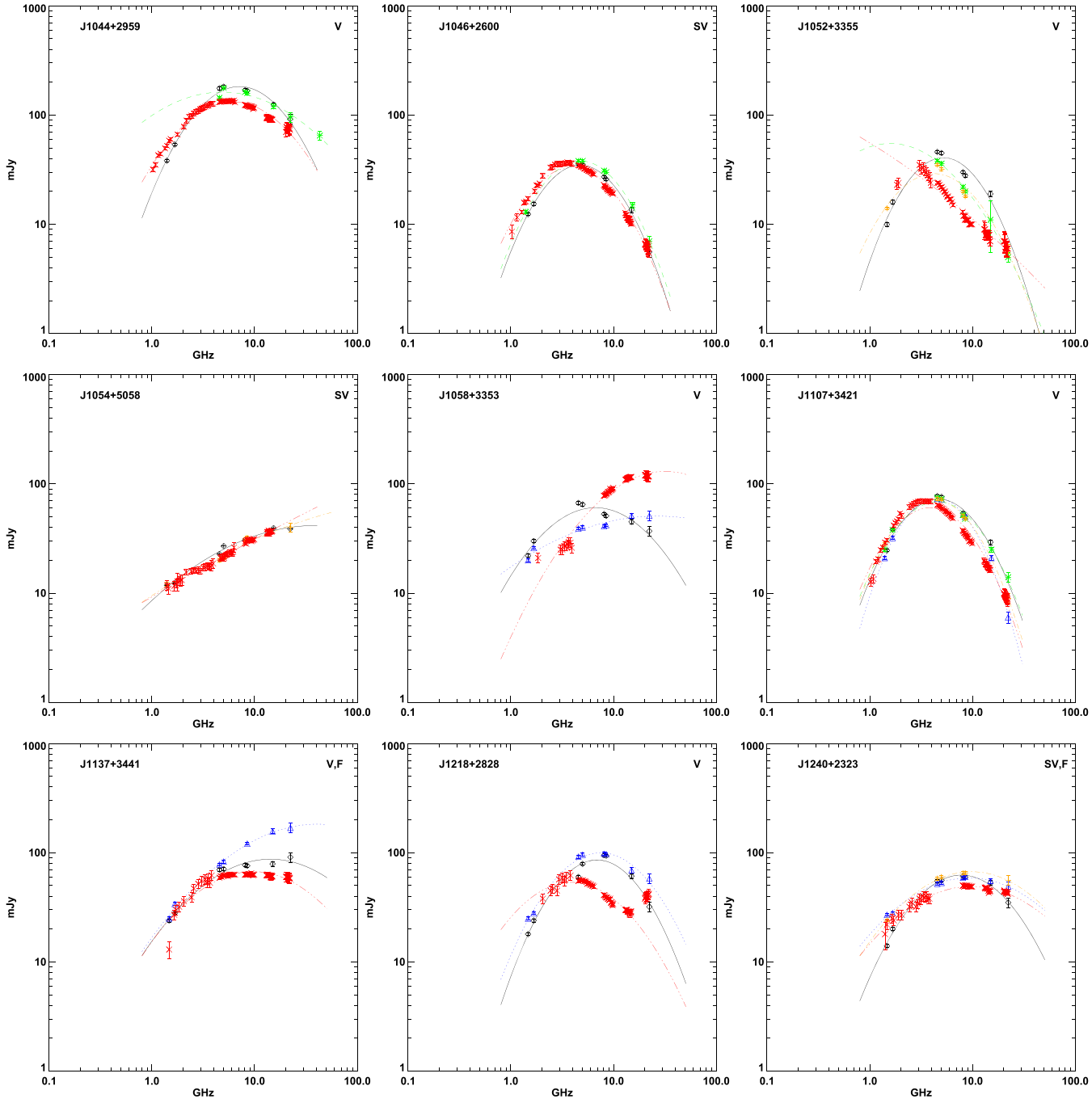

Figure 1 – *continued*

Sloan Digital Sky Survey (SDSS) information from the data release 12 (DR12; Alam et al. 2015) has been used to identify the host and its redshift (either spectroscopic or photometric) of the sources still lacking an optical counterpart in previous studies. The updated information is reported in Table 2.

3.1 Radio spectrum

One of the main characteristics of young radio sources is the convex radio spectrum that turns over at a frequency related to the source size/age. In general, as the source deploys in the interstellar medium (ISM) of the host galaxy, the peak frequency progressively moves to lower and lower frequencies. The anticorrelation found between the peak frequency and the linear size (O'Dea & Baum 1997) implies that the smaller and younger sources should have the spectral peak above a few GHz.

Following Orienti & Dallacasa (2010) and with the goal of estimating the peak frequency and how it changes with time, we fitted the simultaneous multifrequency radio spectrum for each epoch with the pure analytic function:

$$\mathrm{Log}(S) = a + \mathrm{Log}(\nu) \times (b + c\,\mathrm{Log}(\nu)), \quad (1)$$

where S is the flux density, ν is the frequency, and a, b, and c are numeric parameters. Fits to the radio spectra are presented in Fig. 1.

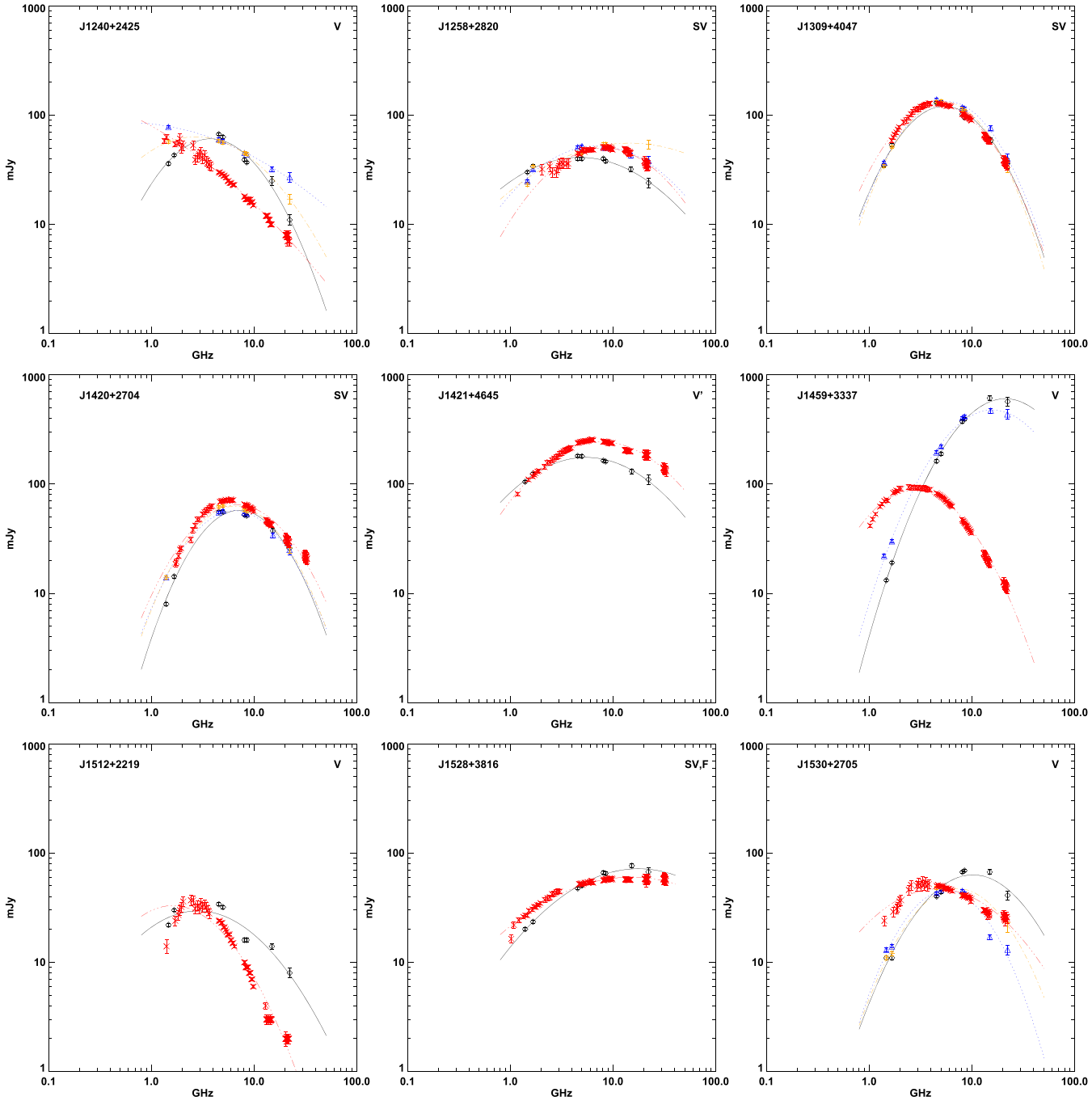

Figure 1 – *continued*

For two sources, J1052 + 3355 and J1512 + 2219 the fit did not converge. In particular, the spectrum of J1512 + 2219 is highly convex, whereas in J1052 + 3355 the lack of data points at low frequencies prevents the fit in the optically thick part of the spectrum.

Following Orienti & Dallacasa (2010), we compute the spectral index below (α_b) and above (α_a) the peak frequency. For some sources, we could not estimate either α_b or α_a, due to the lack of data points above or below the peak frequency.

In 6 sources, J1008 + 2535, J1137 + 3441, J1240 + 2323, J1528 + 3816, J1530 + 5137, and J1616 + 4632, the spectral shape changes from convex in the first epoch to flat in 2012, with $\alpha_a < 0.4$. In addition, the source J1054 + 5058 shows an inverted spectrum up to 24/32 GHz in all epochs. The remaining sources keep a convex spectrum, but with some amount of flux density variation.

In 19 out of the 35 observed sources (54 per cent: 14 quasars, 4 galaxies, and 1 object still missing the optical counterpart), we observe a decrease of the flux density in the optically thin part of the spectrum, and a flux density increase below the actual peak frequency, which may be consistent with a source in adiabatic expansion. Although the variability probed by the VLA monitoring for J0955 + 3335 is consistent with a source in adiabatic expansion, the flux density measured by VLBA images in an intermediate epoch (in 2010) revealed a temporary increase of the flux density at 15 and

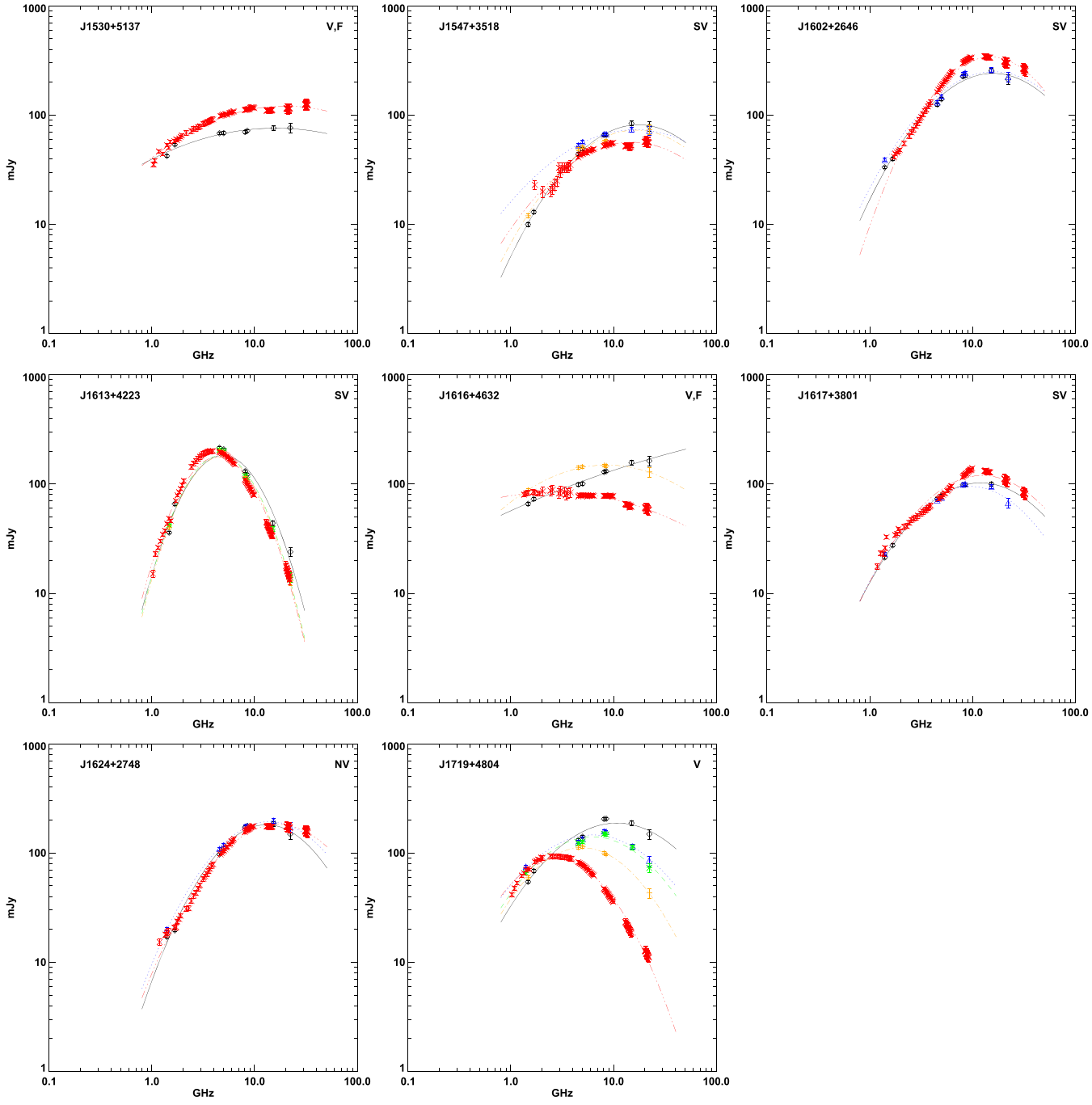

Figure 1 – *continued*

22 GHz, which is hard to reconcile with an expanding source. For this reason, Orienti & Dallacasa (2012) labelled this source a blazar candidate, and we do not consider this source as a CSO candidate anymore. The same reasoning applies to the source J1052 + 3355 (see Section 3.5).

The remaining 16 sources (46 per cent: 9 quasars, 6 galaxies, and 1 object still missing an optical counterpart) show random flux density increase or decrease, as it is expected in blazars.

In Table 5, we provide the peak frequency for each observing epoch. In 13 sources, the peak frequency remains roughly constant, within the errors, while in 11 sources it moves to lower frequencies with time. Among the latter group, the source J1218 + 2828 represents an outlier: between 1.4 and 15 GHz the spectral shape is convex with the peak frequency shifted towards lower frequencies with respect to that estimated in earlier epochs. However, above 15 GHz the flux density increases again, suggesting the presence of an additional compact component with a highly inverted spectrum. The radio spectrum becomes clearly inverted within the 2-GHz bandwidth sampled by the present observations in the *K* band. In four sources, the peak moves to higher frequencies with time, while in five sources it moves up and down without any trend. Remarkably, in all the 18 sources with spectral variability consistent with adiabatic expansion, the peak frequency is constant or decreases with time.

Table 4. VLBA flux density of HFP sources.

Source	Comp	S_{15} mJy	S_{24} mJy	α_{15}^{24}	$\alpha_{\rm VLA}$	F_{15} %	F_{24} %
J0754 + 3033	E	50.7 ± 3.5	38.0 ± 2.7	0.6 ± 0.2	–	–	–
	W	26.0 ± 1.8	14.2 ± 1.0	1.3 ± 0.2	–	–	–
	Tot	79.4 ± 5.5	54.7 ± 3.8	0.8 ± 0.2	0.3 ± 0.3	0.73	0.57
J0819 + 3823	E	4.7 ± 0.3	–	–	–	–	–
	W	21.7 ± 1.5	–	–	–	–	–
	Tot	26.4 ± 1.8	10.4 ± 0.7	2.0 ± 0.2	1.0 ± 0.3	0.64	0.42
J1002 + 5701	Tot	8.0 ± 0.6	3.1 ± 0.2	2.0 ± 0.2	1.0 ± 0.3	0.40	0.24
J1025 + 2541	E	7.8 ± 0.5	–	–	–	–	–
	W	2.0 ± 0.1	–	–	–	–	–
	Tot	9.8 ± 0.7	6.9 ± 0.5	0.7 ± 0.2	1.6 ± 0.5	0.89	1.4
J1035 + 4230	E	–	13.0 ± 0.9	–	–	–	–
	W	–	5.2 ± 0.4	–	–	–	–
	Tot	28.5 ± 2.0	18.2 ± 1.3	1.0 ± 0.2	0.8 ± 0.3	0.48	0.45
J1044 + 2959	Tot	73.8 ± 5.2	45.1 ± 3.1	1.0 ± 0.2	0.5 ± 0.3	0.78	0.60
J1046 + 2600	E	–	5.3 ± 0.4	–	–	–	–
	W	–	4.1 ± 0.3	–	–	–	–
	Tot	11.2 ± 0.8	9.4 ± 0.7	0.4 ± 0.2	1.2 ± 0.3	1.00	0.64
J1107 + 3421	E	4.2 ± 0.5	3.2 ± 0.2	0.6 ± 0.3	–	–	–
	W	3.1 ± 0.5	4.0 ± 0.5	–0.5 ± 0.4	–	–	–
	Tot	7.3 ± 0.7	7.2 ± 0.7	0.0 ± 0.3	1.4 ± 0.3	0.40	0.80
J1420 + 2704	Tot	28.0 ± 2.0	18.4 ± 1.3	0.9 ± 0.2	0.9 ± 0.3	0.62	0.63
J1459 + 3337	E	5.3 ± 0.4	3.3 ± 0.3	1.0 ± 0.3	–	–	–
	W	20.1 ± 1.4	11.5 ± 0.8	1.2 ± 0.2	–	–	–
	Tot	25.4 ± 1.8	14.8 ± 1.0	1.1 ± 0.2	0.9 ± 0.3	0.23	0.22
J1613 + 4223	Tot	28.9 ± 2.0	5.8 ± 0.4	3.4 ± 0.2	1.6 ± 0.4	0.87	0.39
J1719 + 4804	Tot	4.2 ± 0.3	3.5 ± 0.3	0.4 ± 0.2	1.0 ± 0.3	0.23	0.32

Notes. Column 1: source name; column 2: source component; columns 3 and 4: flux density (in mJy) at 15 and 24 GHz, respectively; column 5: VLBA spectral index between 15 and 24 GHz; column 6: VLA spectral index between 15 and 22 GHz; columns 7 and 8: fractional flux density between VLBA and VLA, $S_{\rm VLBA}/S_{\rm VLA}$ at 15 and 24 GHz, respectively. For the source, J1002 + 5701 the VLA spectral index and flux density refers to data from Stanghellini et al. (2009).

3.2 Variability

Samples selected at high radio frequencies (> 5 GHz) have proved to be highly contaminated by blazars (Tinti et al. 2005; Torniainen et al. 2005; Hovatta et al. 2006; Sadler et al. 2006, 2008; Orienti et al. 2007; Mingaliev et al. 2012). Flux density and spectral variability are common properties of blazars, whereas CSOs are among the least variable sources with variability of about 10 per cent at most over one year (O'Dea 1998), while some 'secular' variations are known for a few objects (e.g. OQ 208, Stanghellini et al. 1997).

In order to identify and remove highly variable sources, we performed multiepoch VLA observations covering quasi-simultaneously the frequencies between ∼1 and 22 GHz. Following Tinti et al. (2005), we estimate the variability by means of the parameter V defined as

$$V = \frac{1}{m}\sum_{i=1}^{m}\frac{(S_{\rm A}(i) - S_{\rm B}(i))^2}{\sigma_i^2}, \quad (2)$$

where $S_{\rm A}(i)$ and $S_{\rm B}(i)$ are the flux density at the ith frequency of two consecutive epochs, σ_i is the error on $S_{\rm A}(i) - S_{\rm B}(i)$, and m is the number of sampled frequencies. We compute the variability index on consecutive epochs $V_{\rm ep}$ in order to detect a flaring state followed by a period of quiescence. In addition, we compute $V_{\rm tot}$ between the first epoch from Stanghellini et al. (2009) and last epoch (data presented in this paper) in order to determine the long-term variability spanning a decade of observations (between 1998–1999 and 2012). Results are reported in Table 5. In Fig. 3, we plot the distribution of $V_{\rm tot}$ for galaxies, quasars, and all sources. Values range between about 3 and 255. Only 1 source optically associated with a galaxy (J1624 + 2748) has $V_{\rm tot}$ <4, and is marked as non variable, NV, in Table 5 and in Fig. 1. The threshold $V = 4$ indicates variability of 10 per cent between two epochs. The majority of the objects, ∼47 per cent (16 sources: 13 quasars, 2 galaxies, and 1 object with no optical counterpart) have $V \leq 25$, indicating that some variability, up to about 30 per cent, is common on long time-scales. These sources are marked as slightly variable SV in Table 5 and in Fig. 1. Sources with a variability index above 25 are marked V. If the spectrum turns out to be flat, the source is also labelled F (see Section 3.1).

In Fig. 4, we plot for each source the variability indices computed for consecutive epochs $V_{\rm ep}$ as a function of the variability index computed over the whole period $V_{\rm tot}$. Usually, the variation between two consecutive epochs is smaller than that estimated over the whole period. This is consistent with changes produced by a source in adiabatic expansion. In total, 10 sources (5 quasars, 4 galaxies, and 1 object with an unidentified optical counterpart) have $V_{\rm ep} > V_{\rm tot}$, indicating that the variation observed between two consecutive epochs is larger than the variability derived between 1998−1999 and 2012. This behaviour is typical of blazars, which randomly interchange low-activity and high-activity states.

3.3 Dynamical ages

The radio spectrum of a homogeneous synchrotron source with the magnetic field frozen in the plasma that is in adiabatic expansion shows a flux density increase with time in the optically thick part of

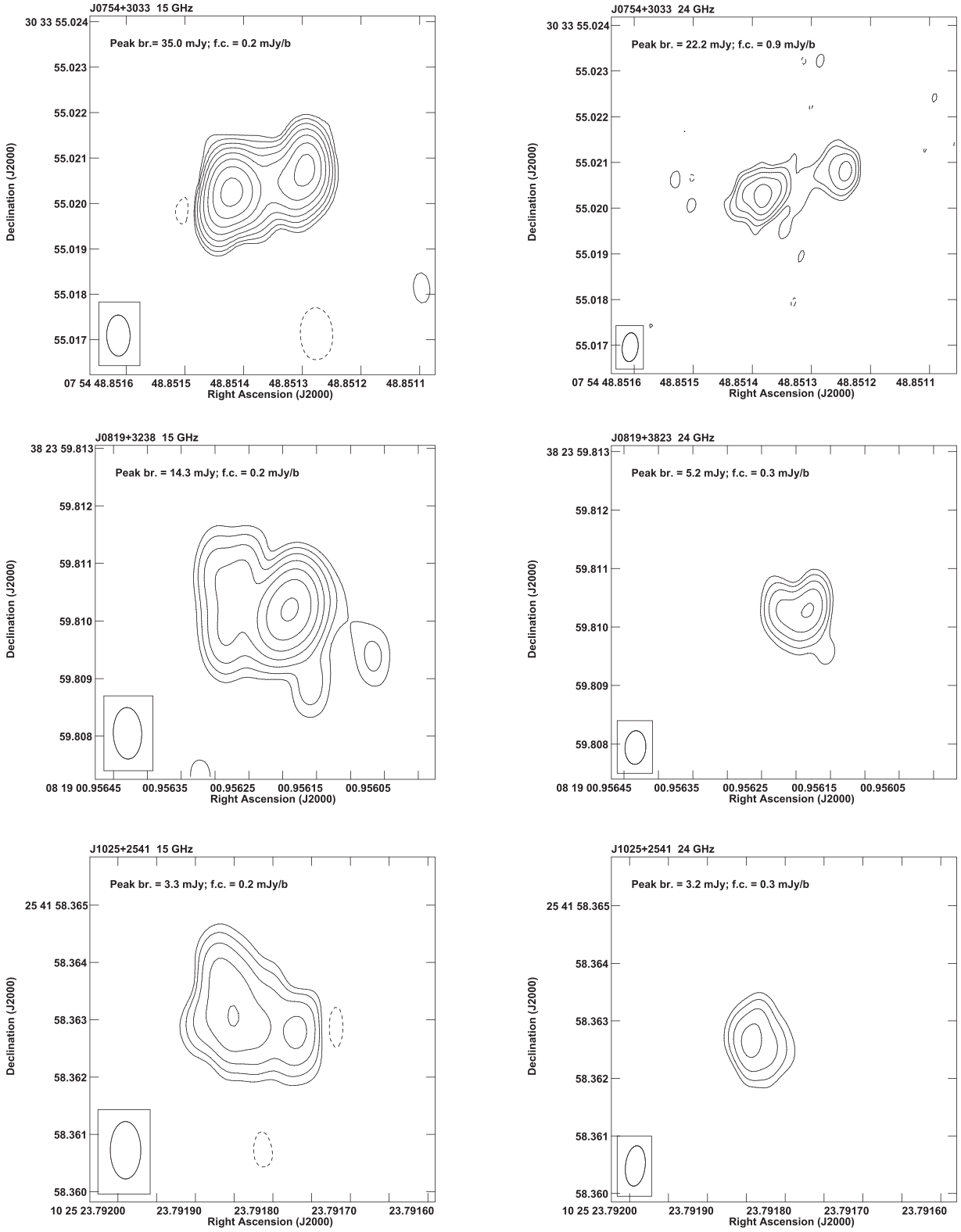

Figure 2. VLBA images at 15 GHz (left-hand panel) and at 24 GHz (right-hand panel). On each image, we provide the source name, the observing frequency, the peak brightness (peak br.) and the first contour (f.c.), which is three times the off-source noise level on the image plane. Contours increase by a factor of 2. The beam is plotted in the bottom left-hand corner of each image.

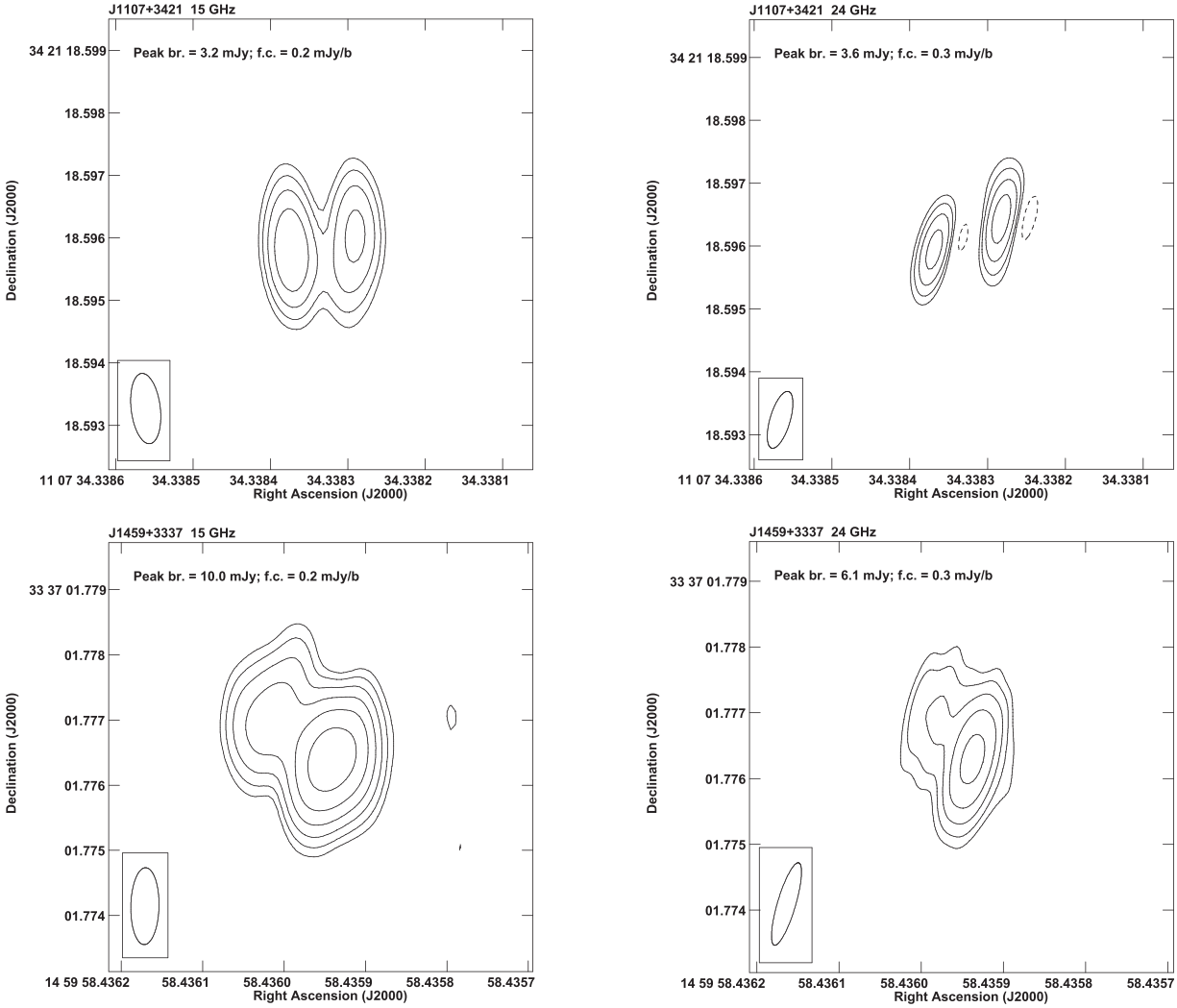

Figure 2 – *continued*

the spectrum:

$$S_1 = S_0 \left(\frac{t_0 + \Delta t}{t_0} \right)^3, \quad (3)$$

where S_0 and S_1 are the flux densities at the time t_0 and $t_0 + \Delta t$, i.e. the source lifetime at the time of the last observing epoch. Moreover, the peak frequency moves towards low frequencies:

$$\nu_{p,1} = \nu_{p,0} \left(\frac{t_0}{t_0 + \Delta t} \right)^4, \quad (4)$$

where $\nu_{p,0}$ and $\nu_{p,1}$ are the flux density at the time t_0 and $t_0 + \Delta t$. Among the 35 sources observed in 2012, 18 sources (14 quasars, 3 galaxies, and 1 object with no optical counterpart) show a variability that is consistent with the expectation of adiabatic expansion. We estimate the dynamic age of the radio source, $t_0 + \Delta t$, using equation (3) and comparing the flux density at 1.4/1.7 GHz during the first and last observing epoch. The dynamical age estimated by equation (4) is highly uncertain due to the large uncertainty on the peak frequency. The estimated dynamical age for the 11 sources with significant variability consistent with adiabatic expansion is reported in Table 6. Dynamical ages range between 40 and 270 yr, supporting the idea that these sources are in a very early phase of their evolution. For the remaining seven sources, the variation in the optically thick part of the spectrum is consistent within the errors, preventing us to set any constraints on their age.

3.4 Parsec-scale structure

A sub-sample of 12 sources from the faint HFP sample were observed with the VLBA in 2019 January. These sources were selected on the basis of their peak frequency below 7 GHz in order to have VLBA observations at 15 and 24 GHz in the optically thin part of the spectrum. In total, five sources (about 42 per cent) are resolved into two components, while two sources are marginally resolved at 24 GHz only (Table 3). Among the 12 newly observed sources, 6 were target of earlier VLBA observations at 8.4 and 15 GHz (Orienti & Dallacasa 2008a, 2012). The source J1107 + 3421 is resolved in VLBA images at both epochs, whereas J1002 + 5701 (not observed by VLA in 2012) that turned to be slightly resolved in Orienti & Dallacasa (2012) is now unresolved. Remarkable cases are J0819 + 3823 and J1459 + 3337, which show a double structure in the last epoch of observations, while they were unresolved in earlier observations. J1420 + 2704 and J1613 + 4223 are unresolved in both observing epochs. In general, the flux density at 15 GHz in our VLBA observations in 2019 is significantly smaller than the flux density measured at the same frequency in earlier VLBA observations, in

Table 5. Variability and peak frequency of faint HFP sources.

Source (1)	$V_{ep(1-2)}$ (2)	$V_{ep(2-3)}$ (3)	$V_{ep(3-4)}$ (4)	$V_{ep(4-5)}$ (5)	$V_{tot(1-5)}$ (6)	$\nu_{p,1}$ (7)	$\nu_{p,2}$ (8)	$\nu_{p,3}$ (9)	$\nu_{p,4}$ (10)	$\nu_{p,5}$ (11)	Class. (12)
J0754 + 3033◇	$26.5^{b,d}$	$1.5^{d,e}$	$1.9^{e,f}$	$6.1^{f,h}$	57.4	8.8 ± 0.6	7.8 ± 0.4	8.3 ± 0.5	7.4 ± 0.2	6.5 ± 1.0	V
J0819 + 3823◇	$6.1^{a,d}$	$2.7^{d,e}$	$8.5^{e,f}$	$13.5^{f,h}$	7.4	6.1 ± 0.9	5.7 ± 1.0	6.0 ± 0.9	6.2 ± 0.9	5.6 ± 1.9	SV
J0821 + 3107◇	$52.5^{b,f}$	$41.0^{f,h}$	–	–	130.0	3.4 ± 0.3	–	–	2.7 ± 0.3	<2.0	V
J0951 + 3451◇	$0.2^{a,d}$	$4.0^{d,f}$	$2.7^{f,h}$	–	12.6	6.1 ± 0.5	6.0 ± 0.6	–	5.6 ± 0.5	5.6 ± 1.0	SV
J0955 + 3335	$6.2^{b,d}$	$9.7^{d,f}$	$9.8^{f,h}$	–	124.1	5.7 ± 0.6	5.2 ± 0.5	–	4.6 ± 0.4	2.4 ± 0.4	V
J1008 + 2533	$17.8^{a,e}$	$1.4^{e,f}$	$3.4^{f,h}$	–	19.7	5.9 ± 0.5	–	4.9 ± 0.4	5.4 ± 0.4	4.1 ± 0.7	SV
J1020 + 4320	$1.7^{b,e}$	$17.7^{e,h}$	–	–	23.3	4.6 ± 0.4	–	4.6 ± 0.5	–	5.2 ± 1.2	SV
J1025 + 2541	$15.2^{a,e}$	$19.7^{e,h}$	–	–	36.9	4.2 ± 0.7	–	3.7 ± 0.5	–	3.3 ± 1.2	V
J1035 + 4230◇	$7.8^{b,e}$	$8.4^{e,h}$	–	–	20.8	7.1 ± 0.6	–	6.7 ± 0.8	–	7.0 ± 1.9	SV
J1044 + 2959◇	$4.1^{b,e}$	$22.6^{e,h}$	–	–	35.9	7.1 ± 0.7	–	4.8 ± 0.3	–	6.1 ± 1.2	V
J1046 + 2600	$4.9^{a,e}$	$22.4^{e,h}$	–	–	13.4	4.7 ± 0.7	–	4.8 ± 0.6	–	4.0 ± 1.3	SV
J1052 + 3355◇	$42.0^{b,e}$	$4.8^{e,f}$	$73.3^{f,h}$	–	206.0	5.2 ± 0.6	–	1.6 ± 0.1	4.2 ± 0.5	<2	V
J1054 + 5058◇	$7.6^{c,f}$	$9.1^{f,h}$	–	–	7.1	>22	–	–	>22	>15	SV
J1058 + 3353	$41.4^{b,d}$	$105.4^{d,h}$	–	–	72.2	6.7 ± 0.6	26.5 ± 0.3	–	–	31.7 ± 0.6	V
J1107 + 3421◇	$14.5^{b,d}$	$8.5^{d,e}$	$2.8^{e,f}$	$22.7^{f,h}$	49.9	4.6 ± 0.6	4.4 ± 0.8	4.6 ± 0.6	4.2 ± 0.6	3.9 ± 1.4	V
J1137 + 3441	$32.5^{b,d}$	$105.4^{d,h}$	–	–	19.3	14.3 ± 0.4	>34	–	–	9.7 ± 0.7	V
J1218 + 2828	$19.5^{a,d}$	$176.2^{d,h}$	–	–	131.2	6.9 ± 0.7	7.5 ± 0.6	–	–	3.9 ± 0.4	V
J1240 + 2323	$6.2^{a,d}$	$4.2^{d,f}$	$20.6^{f,h}$	–	9.4	7.8 ± 0.6	9.3 ± 0.4	–	9.8 ± 0.4	9.8 ± 0.6	SV
J1240 + 2425	$14.8^{a,d}$	$2.6^{d,f}$	$193.0^{f,h}$	–	156.5	3.8 ± 0.5	<1.4	–	2.7 ± 0.3	< 1	V
J1258 + 2820	$21.3^{b,d}$	$4.6^{d,f}$	$3.2^{f,h}$	–	22.9	4.7 ± 0.3	7.0 ± 0.4	–	14.6 ± 0.3	8.1 ± 0.5	SV
J1309 + 4047◇	$7.0^{b,d}$	$1.6^{d,f}$	$5.3^{f,h}$	–	2.4	5.4 ± 0.6	5.7 ± 0.6	–	5.4 ± 0.7	4.8 ± 1.0	SV
J1420 + 2704◇	$8.6^{b,d}$	$2.8^{d,g}$	$6.0^{g,h}$	–	24.6	7.2 ± 0.8	6.5 ± 0.6	6.6 ± 0.6	–	6.9 ± 1.3	SV
J1421 + 4645	–	–	–	–	44.1	5.5 ± 0.3	–	–	–	7.8 ± 1.0	V
J1459 + 3337	$37.3^{b,d}$	$182.2^{d,h}$	–	–	250.8	21.2 ± 0.9	15.8 ± 0.8	–	–	2.8 ± 0.9	V
J1512 + 2219◇	–	–	–	–	92.3	2.8 ± 0.3	–	–	–	1.6 ± 0.5	V
J1528 + 3816	–	–	–	–	19.4	17.7 ± 0.4	–	–	–	15.2 ± 0.7	SV
J1530 + 2705	$58.1^{b,d}$	$4.7^{d,g}$	$20.6^{g,h}$	–	22.9	10.2 ± 0.6	5.6 ± 0.7	–	7.2 ± 0.7	4.6 ± 0.6	V
J1530 + 5137	–	–	–	–	52.7	15.9 ± 0.2	–	–	–	19.9 ± 0.7	V
J1547 + 3518◇	$5.9^{b,d}$	$7.2^{d,f}$	$8.4^{f,h}$	–	23.9	17.5 ± 0.5	16.3 ± 0.1	–	16.4 ± 0.4	14.9 ± 0.6	SV
J1602 + 2646	$3.1^{b,d}$	$22.5^{d,h}$	–	–	28.5	15.9 ± 0.5	16.2 ± 0.5	–	–	15.0 ± 1.5	V
J1613 + 4223◇	$6.7^{b,e}$	$0.8^{e,g}$	$1.2^{g,h}$	–	12.6	4.7 ± 0.8	4.5 ± 0.8	4.5 ± 0.8	–	4.4 ± 2.0	SV
J1616 + 4632	$26.1^{b,f}$	$126.9^{f,h}$	–	–	62.2	>22	–	–	8.6 ± 0.3	2.6 ± 0.2	V
J1617 + 3801	$1.3^{b,d}$	$9.7^{d,h}$	–	–	14.4	12.0 ± 0.4	9.6 ± 0.5	–	–	12.5 ± 1.7	SV
J1624 + 2748◇	$3.8^{b,d}$	$4.7^{d,h}$	–	–	2.7	13.0 ± 0.7	14.2 ± 0.6	–	–	16.9 ± 2.3	NV
J1719 + 4804◇	$27.6^{b,d}$	$2.3^{d,e}$	$34.3^{e,g}$	$120.7^{g,h}$	254.3	10.8 ± 0.4	6.3 ± 0.4	6.2 ± 0.4	4.9 ± 0.4	2.8 ± 0.9	V

Notes. Column 1: source name (sources which are still considered CSO candidates are marked with a diamond); columns 2–5: variability computed between two consecutive epochs, V_{ep} [$a = 1998$, $b = 1999$, $c = 2000$, $d = 2003$, $e = 2004$, $f = 2006$, $g = 2007$, and $h = 2012$. For the precise dates, see Stanghellini et al. (2009) and Orienti & Dallacasa (2010)]. Column 6: variability computed between the first epoch (1998–2000, Stanghellini et al. 2009) and last epoch (2012) of VLA observations, V_{tot}; columns 7–11: peak frequency during the first (1998–1999), second (2003), third (2004), fourth (2006–2007), and last (2012) observing epochs, respectively; column 12: variability classification – NV = non-variable, SV = slightly variable, V = variable (see Section 3.2).

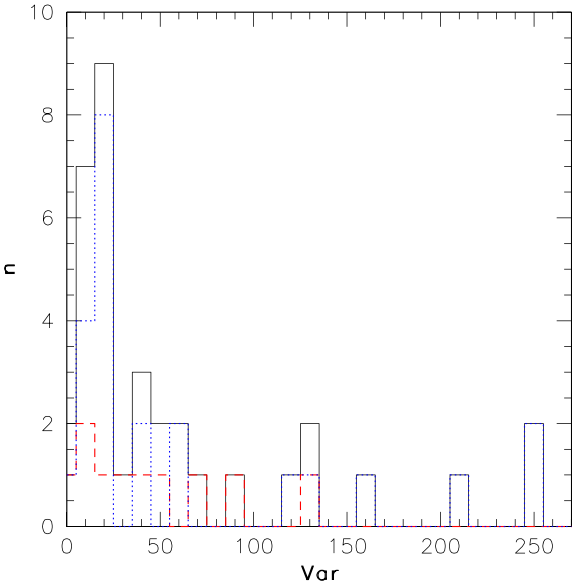

Figure 3. Distribution of the variability index computed over the whole period V_{tot}, for galaxies (red dashed line), quasars (blue dotted line), and all sources (black solid line).

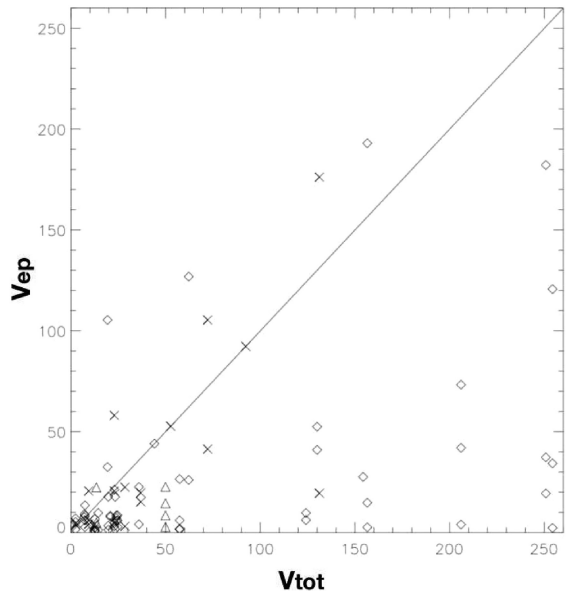

Figure 4. Variability index computed for two consecutive epochs V_{ep} as a function of the variability index computed over the whole period V_{tot} for each source. Crosses, diamonds, and triangles refer to galaxies, quasars, and sources with unidentified optical counterpart, respectively. The line indicates $V_{ep} = V_{tot}$.

agreement with the trend of decreasing flux density observed in the VLA monitoring campaign. Usually S_{VLBA}/S_{VLA} at 15 GHz is comparable or higher than at 24 GHz. In three sources, S_{VLBA}/S_{VLA} is higher at 24 GHz. Although the central frequencies of VLA and VLBA observations are slightly different (14.5 and 21.5 GHz at the VLA and 15 and 24 GHz at VLBA), the flux densities can still be compared. In fact, even in the case of the source with the steepest spectral index (J1613 + 4223, $\alpha_{VLA} \sim 1.6$), the difference between the flux density at 14.5 (21.5) GHz and the one extrapolated at 15 (24) GHz is within the error. The spectral index of the sources has been

Table 6. Estimated dynamical ages for faint HFP sources whose variability is consistent with relativistic plasma in adiabatic expansion.

Source name	Δt (d)	t_{age} (yr)	r (pc)	v c
J0754 + 3033	4713	130	12	0.5
J0819 + 3823	4932	240	–	
J0955 + 3335	4709	240	–	
J1044 + 2959	4576	75	<4	<0.7
J1052 + 3355	4709	100	–	
J1107 + 3421	4709	270	–	
J1309 + 4047	4688	255	6.8	0.4
J1420 + 2704	4596	130	–	
J1459 + 3337	4699	40	7	0.9
J1613 + 4223	4720	225	–	
J1719 + 4804	4720	160	<2.5	<0.1

Notes. Column 1: source name; column 2: the time (in days) elapsed between the first and last VLA observations; column 3: source dynamical age (in yr) at the epoch of last VLA observations in 2012; Column 4: linear size (pc); column 5: estimated source expansion velocity in units of the speed of light.

computed considering the full-resolution images at both frequencies, since they allow the lowest rms noise levels in the images. This may cause an artificial steepening of the spectral index if some extended emission is present. In general, the spectral index ranges between –0.5 and 2.0 (Table 4), indicating the presence of compact and flat components, like core and mini-hotspots, and steep-spectrum emission from jets or mini-lobes.

3.5 Notes on individual sources

Here, we provide a brief description of the sources deserving some discussion. Sources which are considered CSO candidates are marked in boldface. An asterisk indicates that the VLBA observations of the source are presented in this paper.

J0754 + 3033*: The VLA radio spectrum shows moderate variability on long time-scales ($V_{tot} \sim 57$), but shows low variability when consecutive epochs separated by few years or less ($V_{ep} < 2$ between 2003 and 2004, and between 2004 and 2006; Table 5) are considered. The turnover frequency slightly moves to lower frequency, from 8.9 ± 0.6 GHz in 1999 to 6.5 ± 1.0 GHz in 2012. The flux density in the optically thin part of the spectrum decreases with time, whereas it increases in the optically thick part. The dynamical age inferred from its variability is about 130 yr (Table 6). On pc-scale the source shows a double structure (Fig. 2) with the components separated by about 1.6 mas (i.e. about 12 pc at the redshift of the source). The spectral index of the eastern component is 0.6, indicating the presence of freshly injected/accelerated relativistic particles, as one would expect if the component hosts the core and/or a mini-hotspot, whereas it is steeper ($\alpha \sim 1.3$) in the western component (Table 4). These characteristics suggest that this source is a CSO candidate.

J0819 + 3823*: The VLA radio spectrum is marginally variable, with $2.7 < V_{ep} < 14$, and $V_{tot} \sim 7$. The peak frequency is roughly constant within the errors ($\nu_p \sim 6$ GHz), while the flux density increases in the optically thick part of the spectrum and decreases in the optically thin part. The dynamical age computed from its variability is about 240 yr (Table 6). In the VLBA image at 15 GHz, there is diffuse emission on the East of the compact component that dominates the flux density, and the source size is about 1 mas. At 24 GHz the compact component is slightly resolved into two components separated by about 0.4 mas (i.e. the distance between the peak of the two components). The spectral index integrated over

the whole VLBA structure is about 2.0, while the VLA spectral index between 15 and 22 GHz is about 1.0, suggesting the presence of extended steep-spectrum emission (Table 4). The larger $S_{\rm VLBA}/S_{\rm VLA}$ at 15 GHz than at 24 GHz supports this interpretation. The source was unresolved in earlier VLBA observations presented in Orienti & Dallacasa (2012). Although the complicated pc-scale radio structure prevents us from unambiguously classify this source as a CSO, the VLA variability is in agreement with what expected for a source in adiabatic expansion. For this reason, we still consider this object as a CSO candidate.

J0951 + 3451: The VLA radio spectrum is convex in all the three observing epochs and the peak frequency is roughly constant within the errors ($\nu_{\rm p} = 5.6 \pm 1.0$). The source shows low variability ($V_{\rm ep}$ and $V_{\rm tot}$ ∼12) and the flux density increases in the optically thick part of the spectrum, while it slightly decreases in the optically thin part. The source is resolved into three components by VLBA observations, with the central region showing a flat spectral index (Orienti & Dallacasa 2012). These characteristics confirm the source as a CSO.

J1008 + 2533: The VLA radio spectrum had a convex shape only during the first epoch. In the subsequent epochs, the spectrum shows a complex shape, with an inverted part below 5 GHz and a flattening at higher frequencies. However, the variability index has relatively small values $1 < V_{\rm ep} < 18$, and $V_{\rm tot}$ ∼20. At pc-scale, it shows a core-jet structure with a compact component with an inverted spectrum dominating the radio emission (Orienti & Dallacasa 2012). These characteristics confirm the blazar nature of this source.

J1025 + 2541*: The VLA radio spectrum has a convex shape in all the three observing epochs. The source has some moderate variable $V_{\rm ep} \sim 15-20$, and $V_{\rm tot}$ ∼37. The peak frequency determined for each epoch is consistent within the errors, with a hint of decrease from ∼4.2 to ∼3.3 GHz. At 15 GHz the pc-scale structure is resolved into two amorphous components whose peaks are separated by about 1.1 mas (i.e. about 6.5 pc), whereas at 24 GHz it shows a single component roughly coincident with the brightest part of the source visible at 15 GHz. The VLBA flux density at 24 GHz is higher than the flux density observed by the VLA in 2012, suggesting a blazar-like variability.

J1107 + 3421*: The VLA radio spectrum shows moderate variability with $2 < V_{\rm ep} < 23$ and $V_{\rm tot} \sim 50$. The turnover frequency is roughly constant within the errors, whereas the flux density in the optically thick part of the spectrum increases with time. The dynamical age computed from its variability is about 270 yr (Table 6). The pc-scale radio source is characterized by two components (Fig. 2) separated by 1 mas. The source position angle slightly changes from –75° to –80° at 15 and 24 GHz. Although the double structure was already pointed out by Orienti & Dallacasa (2012), the flux density ratio at 15 GHz between the components changed from $S_{\rm E}/S_{\rm W}$ ∼2 to 1.3 in 2010 and in 2019, respectively. The spectral index of the eastern component is about 0.6, while in the western component α =–0.5 ± 0.4, indicating an inverted spectrum. This component may be either the core or a very compact self-absorbed hotspot, like in the case of the HFP sources J1335 + 5844 and J1735 + 5049 (Orienti & Dallacasa 2014). The fractional flux density $S_{\rm VLBA}/S_{\rm VLA}$ is higher at 24 GHz than at 15 GHz (about 80 and 40 per cent at 24 and 15 GHz, respectively). On the basis of the VLA variability and the pc-scale properties, we still consider this source as a CSO candidate.

J1309 + 4047: The VLA radio spectrum is roughly constant with $1 < V_{\rm ep} < 7$ and $V_{\rm tot} \sim 2$. The peak frequency is constant within the errors (∼4.5 GHz). The dynamical age computed from the variability is about 255 yr (Table 6). On pc-scale, the source shows a double structure whose components are separated by about 0.8 mas, i.e. 6.8 pc at the redshift of the source (Orienti & Dallacasa 2012). The steep spectral index derived from VLBA data makes us consider this object a CSO candidate.

J1459 + 3337*: This radio source was first identified as an HFP object by Edge et al. (1996) with a turnover frequency of about 30 GHz. In the two decades thereafter, the peak progressively moved to lower and lower frequencies, at about 21 and 15 GHz in 1999 and 2003, respectively, and our new observations in 2012 set the turnover at about 3 GHz. The flux density in the optically thin part of the spectrum progressively decreases with time, while in the optically thick part of the spectrum it steadily increases (the flux density at 1.4 GHz progressively increases from ∼8 mJy in 1993 to ∼50 mJy in 2012). The source displays one of the highest variability index $V_{\rm tot}$ ∼250. The dynamical age computed from its variability is about 40 yr (Table 6). We observed a change in the radio morphology of this source: it was unresolved in VLBA observations in 2005 (Orienti & Dallacasa 2008a), while in our new observations it shows a double structure (Fig. 2) with the two components separated by about 1.1 and 0.9 mas at 15 and 24 GHz, respectively (i.e. about 7 pc at the distance of the source). The flux density ratio is $S_{\rm W}/S_{\rm E} \sim 3.8$ and 3.4 at 15 and 24 GHz, respectively. The spectral index is relatively steep, with α ∼1.0 and ∼1.2 in the eastern and western component, respectively. This source shows one of the largest discrepancies between VLA and VLBA flux density, $S_{\rm VLBA}/S_{\rm VLA} \sim 20$ per cent at both frequencies, indicating a huge flux density decrement between 2012 and 2019 with no significant variation of the spectral shape between these frequencies (Table 4). Spectral and morphological changes may be explained in terms of either a CSO or a knot that is moving downstream along the approaching jet. In the first scenario, the two components may be two asymmetric mini-lobes that are moving away from each other. However, if we consider that the source grows from <0.3 mas (<2 pc) in 2005 to 1 mas (about 7 pc) in 2019, we infer a source expansion of about c, favouring the interpretation of the propagation of a knot along the approaching jet that was produced by a huge flare a few decades ago in a moderately beamed radio source. Although the variability associated with a single event hardly lasts longer than a few years (Hovatta et al. 2008), there are some cases in which the ejected component can be followed for longer time. An example is 3C 84, which underwent a huge increase of flux density in the 1960s, followed by the ejection and expansion of the southern jet (Walker, Romney & Benson 1994: Asada et al. 2006), whereas not much can be said for the northern counterpart due to severe free–free absorption that prevents its detection below 22 GHz. A similar situation may have happened in the case of J1459 + 3337, where the component emerging from the main compact region may be the approaching jet. This interpretation may be supported by the slightly different position of the eastern component in our images at 15 and 24 GHz with respect to the brightest one. For these reasons, we consider J1459 + 3337 a blazar-like candidate.

J1530 + 2705: The VLA radio spectrum shows moderate variability $4 \leq V_{\rm ep} < 60$ and $V_{\rm tot} \sim 23$. Changes of the peak frequency and of flux density in the optically thick and in the optically thin part of the spectrum do not follow any trend with time. This radio source is hosted in a nearby galaxy, which is part of a group (Orienti & Dallacasa 2010). No information on the pc-scale structure is available, but the erratic variability suggests that this source is a blazar.

J1613 + 4223*: The VLA radio spectrum is highly convex with $\alpha_{\rm b} = -1.9$ and $\alpha_{\rm a} = 1.6$, and shows a modest variability $0.8 \leq V_{\rm ep} < 16$ and $V_{\rm tot} \sim 13$. The dynamical age estimated by the variability is about 225 yr (Table 6). The peak frequency is constant within

the errors (∼4.5 GHz). On pc-scale the source is unresolved at both 15 and 24 GHz, with an upper limit on its angular size of 0.4 mas. The spectral index of the whole source is very steep, suggesting the presence of steep-spectrum low-surface brightness emission that may have been missed at 24 GHz as supported by the much larger $S_{\rm VLBA}/S_{\rm VLA}$ observed at 15 GHz than at 24 GHz (Table 4). On the basis of the VLA variability that is consistent with a source in adiabatic expansion, we still consider this source as a CSO candidate.

J1624 + 2748: The VLA radio spectrum is convex and displays one of the lowest variability estimated for this sample with $V_{\rm ep} \sim 4$ and $V_{\rm tot} \sim 3$. The peak frequency is roughly constant within the errors. No information on pc-scale structure is available, but the variability properties make this object a very promising CSO candidate.

J1719 + 4804*: The radio spectrum is convex and displays high variability with $V_{\rm tot} \sim 254$. The peak frequency shifts from 10.8 to 2.8 GHz from 1999 to 2012. The dynamical age computed from the variability is about 160 yr (Table 6). The pc-scale structure is unresolved in our VLBA images, giving an upper limit on the angular size of 0.3 mas, which corresponds to a linear size of 2.5 pc at the redshift of the source. The VLBA flux density at 15 and 24 GHz is about 4 and 3.5 mJy, respectively, indicating a further decrease with respect to that observed in 2012. The VLBA spectral index is rather flat $\alpha = 0.4 \pm 0.2$, suggesting that the radio emission is dominated by the core or a very compact self-absorbed hotspot, like in the case of the HFP sources J1335 + 5844 and J1735 + 5049 (Orienti & Dallacasa 2014). This source shows one of the largest discrepancies between VLBA and VLA flux densities with $S_{\rm VLBA}/S_{\rm VLA} \sim 20$ and 30 per cent at 15 and 24 GHz, respectively, indicating a huge flux density decrement between 2012 and 2019 with a slight variation of the spectral shape between these frequencies (Table 4). The VLA variability consistent with what is expected in case of adiabatic expansion, and the lack of unambiguous blazar characteristics, make us still consider this source as a CSO candidate.

4 DISCUSSION

Ideally, unbeamed young radio sources are characterized by a low level of flux density variability, low fractional polarization, and a double/triple structure dominated by lobe/hotspot components when studied with sub-arcsecond resolution. The location of the source core at the centre of a two-sided radio structure would be the hallmark of a CSO. In contrast, blazars show significant variability, have pc-scale core-jet structures, and high and variable fractional polarization. It is therefore clear that the study of variability, morphology, and polarization is the key to disentangle the nature of a radio source.

HFP sources are all unresolved by arcsecond scale VLA observations and higher resolution observations are necessary for investigating their structure. With the aim of determining the source structures, the optically thin emission of 23 sources from the faint HFP sample has been observed with the VLBA, in 2010 and 2019, and results are reported in Orienti & Dallacasa (2012) and in this paper. Despite the pc-scale resolution, 14 out of the 23 observed sources with VLBA observations are unresolved or marginally resolved. The optically thin spectral index derived from VLA data (Table 2 and Orienti & Dallacasa 2010) points out that 3 of these sources (J1002 + 5701, J1436 + 4820, and J1613 + 4223) have $\alpha_{\rm a} > 1.0$, suggesting that the emission is dominated by steep-spectrum emission, likely from mini-lobes. Among the sources with resolved structure, five sources (J0754 + 3033, J0943 + 5113, J0951 + 3451, J1107 + 3421, and J1135 + 3624) have a double/triple structure that is consistent with those of CSOs, whereas for the other sources the double morphology may be interpreted in terms of either mini-lobes/hotspots or core-jet structure. In general, the detection of only two components makes the classification of these sources rather tentative (e.g. Snellen, Schilizzi & van Langevelde 2000b; Deller & Middelberg 2014). J0951 + 3451 shows slight variability between the first and last epoch, whereas J0754 + 3033 and J1107 + 3421 are highly variable. The other two sources were found non-variable by Orienti & Dallacasa (2010), and the lack of VLA observations in 2012 prevents us from the study of their long-term variability.

Monitoring campaigns of HFPs objects show that moderate variability is a common characteristics of these objects. Earlier studies of the sources from the faint HFP samples pointed out that about 40 per cent of the target sources are non-variable (Orienti & Dallacasa 2010). This percentage drastically decreases to 1 object out of 35 (3 per cent) when we consider a longer time separation between the observing epochs. Contrary to what is found for other samples of high-frequency peakers, among the sources showing a random variability typical of beamed objects, there is a predominance of radio sources associated with galaxies (∼60 per cent) rather than quasars (∼43 per cent).

4.1 Variability in young radio sources

Flux density and spectral variability are not common features of the class of CSOs, but they are the characteristics of blazars. Samples selected at high frequencies (in the GHz regime) are more contaminated by beamed objects than samples selected at lower frequencies or with different criteria (e.g. Coppejans et al. 2016). Variability studies are thus used to discriminate between CSOs and blazars. However, significant variability may be observed also among the youngest CSOs in which freshly produced bubbles of magnetized plasma are expanding in a rather inhomogeneous ambient medium, implying an irregular expansion rate. Moreover, in CSOs the time elapsed between the first and last epoch of the monitoring campaign corresponds to a significant fraction of the lifetime of the radio source. It is then quite likely to observe spectral and flux density changes. Dynamical ages estimated on the basis of the variation of the optically thick flux density range between 40 and 270 yr, supporting the idea that these sources are in a very early phase of their evolution. The values derived in this way should be representative of the order of magnitude of the dynamical ages, owing to the strong assumption of a single homogeneous component that is expanding with no effects from the ambient medium. Moreover, the core activity might not be continuous, and its likely erratic on-off cycle could perturb the predicted flux density variability.

If these sources are actually in a very early stage of their evolution, their large-scale counterpart should be sought among low-power radio sources observed in the MHz regime. In fact, at least for those sources for which it is possible to 'see' the epoch-by-epoch evolution, from equation (4) we expect that the peak frequency would lower by a factor of about 16 as Δt approaches t_0, falling in the MHz regime. In parallel, the optically thin flux density decreases as

$$S_1 = S_0 \left(\frac{t_0 + \Delta t}{t_0} \right)^{-2\delta}, \quad (5)$$

where S_0 and S_1 are the flux densities at the time t_0 and $t_0 + \Delta t$, i.e. the source lifetime at the time of the last observing epoch, and δ is the spectral index of the electron energy distribution of the relativistic particles [$N(E) \propto E^{-\delta}$, $\delta = 2\alpha + 1$]. If in equation (5), we consider typical values for δ between 2 and 3, we find that the flux density would decrease by a factor of about 16−60, becoming of (sub-)mJy level. Only the flux density below the peak frequency becomes more prominent with time. Part of these sources may be progenitors of

the population of low-power radio sources (see Baldi, Capetti & Giovannini 2015, 2019; e.g. Tingay & Edwards 2015; Mingo et al. 2019) and/or MHz-peaked spectrum radio sources (Coppejans et al. 2015), or they may represent short-lived episode of radio emission from an active galactic nucleus (Czerny et al. 2009). The Square Kilometre Array, with its huge improvement in sensitivity in the MHz regime would enable systematic studies of population of faint radio sources, providing a fundamental step in our understanding of their evolution.

For the sources with information on their parsec-scale structure and redshift, we estimate the expansion speed v by

$$v = \frac{\theta\ \mathrm{D_L}}{(1+z)^2}\frac{1+z}{\mathrm{t_{age}}}, \quad (6)$$

where θ is the angular size measured from VLBA images, D_L is the luminosity distance of the source, z is the redshift, and t_age is the estimated dynamical age.

The expansion speed ranges between $0.1c$ and $0.7c$, in agreement with values estimated for the population of CSOs (see e.g. Polatidis & Conway 2003; An & Baan 2012), with the only exception of the quasar J1459 + 3337, which turned out to be likely a blazar on the basis of the pc-scale structure. Owing to the uncertainty on the source age, the expansion speed should be considered as an upper limit. For all the sources our VLBA observations could not identify the core region preventing us from investigating if both jets are expanding at the same velocity or if the ambient medium plays a role in their growth. Jet–cloud interaction seems to be common during the first evolutionary phase when the jet is piercing its way through the dense and inhomogeneous gas of the narrow-line region (Dallacasa et al. 2013). The presence of an inhomogeneous ambient medium has been found in some CSOs from the bright HFP sample (Dallacasa et al. 2000), where free–free absorption is observed towards only one of the two jets/mini-lobes (e.g. J0428 + 3259 and J1511 + 0518, Orienti & Dallacasa 2008b) and highly asymmetric structures mark the presence of clouds slowing down the expansion on one side, preventing its adiabatic expansion and enhancing synchrotron losses (e.g. J1335 + 5844, Orienti & Dallacasa 2014). However, the sources studied so far are relatively powerful ($L_{1.4\mathrm{GHz}} > 10^{26}$ W/Hz), and there are only a few studies on the effects the ambient medium has on the expansion of low power ($L_{1.4\mathrm{GHz}} < 10^{26}$ W/Hz) jets (e.g. Kunert-Bajraszewska et al. 2012). Deep and systematic VLBI observations are necessary for investigating the role of the ambient medium during the first phase of the source expansion in faint objects.

4.2 Steep spectral shape

About 20 per cent (7 out of 35) of the sources discussed here have a rather steep optically thin VLA spectrum ($\alpha_\mathrm{a} > 1.0$), which is quite uncommon in radio galaxies with active regions. These small and compact radio sources have somehow different characteristics with respect to common extended radio galaxies. The equipartition magnetic fields increases as we consider smaller and smaller sources: from a few μG in the lobes of the classical FR-I/II sources (Croston et al. 2005) to a few mG in compact steep-spectrum sources (Fanti et al. 1995), and up to a few tens/hundreds mG in young HFP objects (Orienti & Dallacasa 2008b). This implies that for a given observing frequency, the Lorentz factor of the radiating particle is smaller than in larger sources with weaker fields. Moreover, the radiative losses are higher, shortening the radiative lifetime of the relativistic electrons and shifting the frequency break at lower and lower frequency. In the small sources, the outer components are usually dominated by bright and compact regions, like mini-hotspots, while no significant emission from the lobes is observed (Tingay & de Kool 2003; Gugliucci et al. 2005; Orienti & Dallacasa 2008b, 2014), supporting the severe losses hypothesis.

Alternatively, the steep spectra might be caused by an injection spectral index that is steeper than what is usually found (Harwood et al. 2016, 2017). Deep VLBI observations are necessary to unveil the presence of low-luminosity extended structures and disentangle between the two scenarios.

5 SUMMARY

In this paper, we presented results on a multiepoch multifrequency VLA monitoring campaign, and pc-scale VLBA observations of CSO candidates from the faint HFP sample. The conclusions that we can draw from this investigation are as follows:

(i) In total, 5 out of the 12 sources (42 per cent) observed with milliarcsecond resolution turned out to be compact doubles. Taking into account earlier observations of additional 11 objects, we end up with a total of 11 sources showing a morphology consistent with what is expected for young radio sources. However, the radio structure and the spectral index information are not conclusive and deeper pc-scale observations are necessary to probe the nature of the sources and identify the locations of the centre of activity.

(ii) In total, 34 out of the 35 sources (97 per cent) observed with VLA have moderate to strong long-term variability. Only one source, J1624 + 2748, has neither spectral nor flux density variability.

(iii) In total, 18 radio sources possess spectral and flux density variability that is consistent with a cloud of homogeneous magnetized relativistic plasma in adiabatic expansion. For the sources with known redshift, we estimate the dynamical ages which range between a few tens to a few hundred years. The corresponding expansion velocity is mainly between $0.1c$ and $0.7c$, similar to values found in young radio sources. However, among these sources, one object shows pc-scale properties and an estimated velocity of about c, suggesting a blazar nature.

(iv) In 17 sources, the flux density changes randomly as it is expected in blazars, and in six sources the spectrum becomes flat in the last observing epoch, confirming that samples selected in the GHz regime are highly contaminated by beamed objects.

(v) No significant dichotomy is found in the flux density variability between galaxies and quasars, with a slightly larger fraction of galaxies showing erratic variability typical of beamed sources.

The fast evolution that we observe in some CSO candidates suggests that they hardly represent the progenitors of classical Fanaroff–Riley radio galaxies. Thanks to the huge improvement in sensitivity and the wide frequency coverage up to 100 GHz, the Next Generation Very Large Array[1] will be the optimal instrument for shedding a light on the nature and fate of these objects.

ACKNOWLEDGEMENTS

We thank the anonymous referee for reading the manuscript carefully and making valuable suggestions. The VLA and VLBA are operated by the US National Radio Astronomy Observatory, which is a facility of the National Science Foundation operated under cooperative agreement by Associated Universities, Inc. This work has made use of the NASA/IPAC Extragalactic Database NED, which is operated by the JPL, Californian Institute of Technology, under

[1] ngvla.nrao.edu

contract with the National Aeronautics and Space Administration. AIPS is produced and maintained by the National Radio Astronomy Observatory, a facility of the National Science Foundation operated under cooperative agreement by Associated Universities, Inc. Funding for SDSS-III has been provided by the Alfred P. Sloan Foundation, the Participating Institutions, the National Science Foundation and the US Department of Energy Office of Science. The SDSS-III web site is http://www.sdss3.org/. SDSS-III is managed by the Astrophysical Research Consortium for the Participating Institutions of the SDSS-III Collaboration including the University of Arizona, the Brazilian Participation Group, Brookhaven National Laboratory, Carnegie Mellon University, University of Florida, the French Participation Group, the German Participation Group, Harvard University, the Instituto de Astrofisica de Canarias, the Michigan State/Notre Dame/JINA Participation Group, Johns Hopkins University, Lawrence Berkeley National Laboratory, Max Planck Institute for Astrophysics, Max Planck Institute for Extraterrestrial Physics, New Mexico State University, New York University, Ohio State University, Pennsylvania State University, University of Portsmouth, Princeton University, the Spanish Participation Group, University of Tokyo, University of Utah, Vanderbilt University, University of Virginia, University of Washington, and Yale University.

DATA AVAILABILITY

The data uderlying this paper are available in the NRAO Data Archive (https://science.nrao.edu/observing/data-archive) with the project codes AO281 and BO057. Calibrated data are available on request.

REFERENCES

Alam S. et al., 2015, ApJS, 215, 12
An T., Baan W. A., 2012, ApJ, 760, 77
Asada K., Kameno S., Shen Z.-Q., Horiuchi S., Gabuzda D. C., Inoue M., 2006, PASJ, 58, 261
Baldi C., Capetti A., Giovannini G., 2015, A&A, 576, 38
Baldi C., Capetti A., Giovannini G., 2019, MNRAS, 482, 2294
Collier J. D. et al., 2018, MNRAS, 477, 578
Coppejans R., Cseh D., Williams W., van Velzen S., Falcke H., 2015, MNRAS, 450, 1477
Coppejans R. et al., 2016, MNRAS, 459, 2455
Croston J. H., Hardcastle M. J., Harris D. E., Belsole E., Birkinshaw M., Worrall D. M., 2005, ApJ, 626, 733
Czerny B., Siemiginowska A., Janiuk A., Nikiel-Wroczyński B., Stawarz Ł., 2009, ApJ, 698, 840
Dallacasa D., Stanghellini C., Centonza M., Fanti R., 2000, A&A, 363, 887
Dallacasa D., Orienti M., Fanti C., Fanti R., Stanghellini C., 2013, MNRAS, 433, 147
Deller A. T., Middelberg E., 2014, AJ, 147, 14
Edge A. C., Jones M., Saunders R., Pooley G., Grainge K., 1996, in I. A. G. Snellen et al., eds, Proceedings of the Second Workshop on GPS and CSS Radio Sources. Leiden Observatory, Leiden, p. 208
Fanaroff B. L., Riley J. M., 1974, MNRAS, 167, 31
Fanti C., Fanti R., Dallacasa D., Schilizzi R. T., Spencer R. E., Stanghellini C., 1995, A&A, 302, 317
Fanti C., Pozzi F., Dallacasa D., Fanti R., Gregorini L., Stanghellini C., Vigotti M., 2001, A&A, 369, 380
Gugliucci N. E., Taylor G. B., Peck A. B., Giroletti M., 2005, ApJ, 622, 136
Harwood J. J. et al., 2016, MNRAS, 458, 4443
Harwood J. J. et al., 2017, MNRAS, 469, 639
Hovatta T., Tornikoski M., Lainela M. Lehto H. J., Valtaoja E., Torniainen I., Aller M. F., Aller H. D., 2006, A&A, 469, 899
Hovatta T., Nieppola E., Tornikoski M., Valtaoja E., Aller M. F., Aller H. D., 2008, A&A, 485, 51
Keim M. A., Callingham J. R., Röttgering H. J. A., 2019, A&A, 628, 56
Kunert-Bajraszewska M., Gawroński M. P., Labiano A., Siemiginowska A., 2010, MNRAS, 408, 2261
McMullin J. P., Waters B., Schiebel D., Young W., Golap K., 2007, in Shaw R. A., Hill F., Bell D. J., eds., ASP Conf. Ser. Vol. 376, Astromical Data Analysis and Systems XVI, Astron. Soc. Pac. San Francisco, p. 127
Mingaliev M. G., Sotnikova Y. V., Torniainen I., Tornikoski M., Udovitskiy R. Y., 2012, A&A, 544, 25
Mingo B. et al., 2019, MNRAS, 488, 2701
Morganti R., Fogasy J., Paragi Z., Oosterloo T., Orienti M., 2013, Science, 341, 1082
Murgia M., 2003, PASA, 20, 19
Murgia M., Fanti C., Fanti R., Gregorini L., Klein U., Mack K.-H., Vigotti M., 1999, A&A, 345, 769
O'Dea C. P., 1998, PASP, 110, 493
O'Dea C. P., Baum S. A., 1997, AJ, 113, 148
Orienti M., Dallacasa D., 2008a, A&A, 477, 807
Orienti M., Dallacasa D., 2008b, A&A, 487, 885
Orienti M., Dallacasa D., 2012, MNRAS, 424, 532
Orienti M., Dallacasa D., 2014, MNRAS, 438, 463
Orienti M., Dallacasa D., Tinti S., Stanghellini C., 2006, A&A, 450, 959
Orienti M., Dallacasa D., Stanghellini C., 2007, A&A, 475, 813
Orienti M., Dallacasa D., Stanghellini C., 2010, MNRAS, 408, 1075
Orrú E., Murgia M., Feretti L., Govoni F., Giovannini G., Lane W., Kassim N., Paladino R., 2010, A&A, 515, A50
Polatidis A. G., Conway J. E., 2003, PASA, 20, 69
Readhead A. C. S., Taylor G. B., Pearson T. J., Wilkinson P. N., 1996, ApJ, 460, 634
Sadler E. et al., 2006, MNRAS, 371, 898
Sadler E. M., Ricci R., Ekers R. D., Sault R. J., Jackson C. A., de Zotti G., 2008, MNRAS, 385, 1656
Snellen I. A. G., Schilizzi R. T., Miley G. K., de Bruyn A. G., Bremer M. N., Röttgering H. J. A., 2000a, MNRAS, 319, 445
Snellen I. A. G., Schilizzi R. T., van Langevelde H. J., 2000b, MNRAS, 319, 429
Sobolewska M., Siemiginowska A., Guainazzi M., Hardcastle M., Migliori G., Ostorero L., Stawarz Ł., 2019, ApJ, 871, 71
Stanghellini C., Bondi M., Dallacasa D., O'Dea C. P., Baum S. A., Fanti R., Fanti C., 1997, A&A, 318, 376
Stanghellini C., Dallacasa D., Orienti M., 2009, AN, 330, 223
Tingay S. J., de Kool M., 2003, ApJ, 126, 723
Tingay S. J., Edwards P. G., 2015, MNRAS, 448, 252
Tinti S., Dallacasa D., de Zotti G., Celotti A., Stanghellini C., 2005, A&A, 432, 31
Torniainen I., Tornikoski M., Lähteenmäki A., Aller M. F., Aller H. D., Mingaliev M. G., 2005, A&A, 469, 451
Walker R. C., Romney J. D., Benson J. M., 1994, ApJ, 430, 45
Wilkinson P. N., Polatidis A. G., Readhead A. C. S., Xu W., Pearson T. J., 1994, ApJ, 432, 87

This paper has been typeset from a TEX/LATEX file prepared by the author.